# ISTITUTO NAZIONALE DI RICERCA METROLOGICA
# Repository Istituzionale

Decoration of laser induced graphene with MXene and manganese oxide for fabrication of a hybrid supercapacitor

*Publisher copyright*

(Article begins on next page)

19 September 2024

# Decoration of laser induced graphene with MXene and manganese oxide for fabrication of a hybrid supercapacitor

Marco Reina [a,b,*], Mara Serrapede [a,b], Pietro Zaccagnini [a,b], Alessandro Pedico [a,b], Micaela Castellino [a], Stefano Bianco [a], Thierry Ouisse [c], Hanna Pazniak [c], Jesus Gonzalez-Julian [d,e], Andrea Lamberti [a,b]

[a] Politecnico di Torino, Dipartimento di Scienza Applicata e Tecnologia (DISAT), Corso Duca degli Abruzzi, 24, 10129, Turin, Italy
[b] Istituto Italiano di Tecnologia, Center for Sustainable Future Technologies, Via Livorno, 60, 10144, Turin, Italy
[c] Université Grenoble Alpes, CNRS, Grenoble INP, LMGP, F-38000 Grenoble, France
[d] Forschungzentrum Jülich GmbH, Institute of Energy and Climate Research, Materials Synthesis and Processing (IEK-1), 52428 Jülich, Germany
[e] Department of Ceramics, Institute of Mineral Engineering, RWTH Aachen University, D-52074 Aachen, Germany

## ARTICLE INFO

## ABSTRACT

During the last years, Internet of Things has become a prominent topic of technical, social, and economic importance. One of the main consequences is the high demand for energy and power density from small energy storage devices. In this field the laser induced graphene (LIG) has become a promising material to produce flexible micro-supercapacitors. The issue with this material is that the performances are strongly restrained by its limited surface area and the relatively low conductivity. In this work we improve the performance of a LIG supercapacitor by decorating its surface through electrophoresis: one electrode will be decorated with metal nitrides and metal carbides (MXenes), the other with manganese oxide. These two materials have appreciable conductivity and pseudocapacitance. Electrochemical measurements have been carried out on the two electrodes separately. After a charge balancing, the device has been sealed in pouch and tested.

## 1. Introduction

The rapid development of communication protocols and the widespread of sensing apparatuses in the Internet of Things (IoT) and the increasing demand for wearable and flexible electronics have led to the increased demand for miniaturized energy storage devices (ESDs).

Even though electronics is pushing towards ultra-low power consumption systems, the energy storage community is still looking toward the increase in integrated energy and power densities [1–3]. On one side, micro-batteries are developed to bring high energy densities in reduced volumes. On the other side, micro-supercapacitors (μSC) and more in general capacitive technologies are currently under development to provide solutions with relatively increased energy densities and high-power capabilities. Batteries and SC are complementary technologies that can either co-exist in symbiosis as merged energy storage systems (ESSs) able to provide high energy and power densities, or that can be selected as sole ESSs in specific applications. Among ESDs, μSC are the ones more developed with aqueous electrolytes, which is a key

advantage for safety issues [4–6].

Increasing the energy density of μSC can be achieved via hybrid technology architecture, exploiting different materials with different energy storage properties [7]. SC materials can be divided into electrical double-layer (EDL), pseudocapacitive, and battery-like materials. EDL materials rely on a charge storage mechanism based on electrostatic interactions between the electrodes' charges and ions in solutions. Pseudocapacitive and battery-like materials working principles are based on faradic interactions between the electrode and the electrolyte. These faradic interactions are surface limited in the case of pseudocapacitive materials and diffusion controlled in the case of battery-like materials [8,9]. Combinations of materials for a given electrolyte solution allow expanding electrodes capacities and spreading of the voltage window resulting in an increased energy density. The design of such architectures requires electrodes' charge balancing to exploit at most the achievable voltage window [10,11].

The current world policies and trends concerning energy foresee decarbonization. For this reason, to reduce the environmental impact of

fabricated micro ESD, the development of electro-assisted methods such as electrodeposition and electrophoresis might reduce the overall device's environmental impact [12] together with the developing of aqueous electrolyte-based devices. Another important emerging technological process is the laser conversion of polymers, mainly polyimide (PI), into conductive carbon materials. In recent years the so-called laser-induced graphene (LIG) has been widely studied for diverse applications [13–16]. The photo-chemo-thermal laser-induced phenomenon has been demonstrated to produce conductive materials based on short-range ordered graphene-based structures [17]. The material itself can be exploited for energy storage applications, or it can be exploited to produce relatively high surface area current collectors with improved storage capabilities [18,19]. The use of this technological process opens the possibility to reduce the number of processing steps for miniaturized devices, hence the overall environmental impact. Further, the substrate flexibility is preserved allowing the production of flexible devices.

In the present work, we propose a hybrid μSC based on asymmetrical electrodes based on LIG current collectors. On the anode side, manganese oxide is electrodeposited *via* a supported $Mn^{2+}$ solution, whereas on the cathode side the electrode energy density is increased by means of MXene deposited via electrophoresis. The chosen architecture relies on the manganese material availability and on the MXene electrochemical properties as cathode materials for aqueous-based SCs. Similar architectures have been recently proposed in the recent literature, but none are based on the selected architecture on Kapton as a flexible substrate [20,21].

Manganese oxide and hydroxide have been widely studied as pseudocapacitive materials among the different transition metal oxides (TMO) [22–24]. Their allotropic forms can be obtained by changing the synthesis routes or during the electrochemical processes [25–29]. Since its very first reports [30,31], manganese oxide has shown remarkable specific capacitances considering its theoretical value of 1370 F $g^{-1}$ [32]. In some literature results it is exploited in symmetrical configurations [33–35] but it has been proven as anodic material for SCs [31,36, 37]. A further limitation for the μSC relies on the kind of material placed at the cathode due to the usual small capacity, in which the discharge of ions is compensated by transition-metal redox reactions. Additionally, to those reactions, also oxygen-redox reactions of oxide cathodes have been recognized as an effective way to overcome the capacitive limit, but irreversible changes that occur during charge/discharge cause structural degradation increasing the voltage drops and reducing the cycle lifetime. Here, the redox storage arises from three manganese oxide structures that are $\alpha-Mn_2O_3$, $Na_xMn_2O_4$ and a Mn-defective $Na_2Mn_3O_7$. The latter has been reported to possess a highly reversible oxygen-redox capacity with Mn vacancies in a layered structure [38] and the first is known for its high specific capacitance [39]. $Na_xMn_2O_4$ and $Na_2Mn_3O_4$ have been employed in batteries [40,41], but in this case the crystalline dimensions allow its usage as extrinsic pseudocapacitive material.

MXenes are two-dimensional (2D) transition metal carbide materials offering tunable electrical and electrochemical properties that can be tuned by changing the elemental composition of the Metal-Carbon-Termination (MCT) structure [42,43]. In this work, $Ti_3C_2Cl$ was exploited as cathode active material. Several literature reports proved the effectiveness of MXenes as cathodic materials due to their pseudocapacitive or battery-like behavior [37,44–46]. MXenes features remarkable electrical, mechanical, and electrochemical properties [43, 47]. In the field of supercapacitors MXenes have also been exploited in symmetrical stacked configurations reaching a specific capacitance of 520 F $g^{-1}$ [48].

As for conventional SC architectures, the proposed device is realized in parallel electrode configuration which is still exploitable in μSC.[49, 50] The overall device performance is in line with the perspectives on this class of devices owing to the rated device performance. After the charge balancing design procedure, the rated areal specific capacitance

was 136 mF cm$^{-2}$, the areal energy density was 25.57 μWh cm$^{-2}$ and the areal power was 5.1 mW cm$^{-2}$, rated at a maximum voltage of 1.6 V.

## 2. Experimental

### 2.1. Chemicals

Ethanol $CH_3CH_2OH$ (Sigma Aldrich, 99.8 %) and acetone $CH_3COCH_3$ (Sigma Aldrich, 99.5 %) were used to wash the Kapton © substrates. Manganese acetate $Mn(CH_3COO)_2$ (Alfa Aesar, 98+ %) and sodium sulfate $Na_2SO_4$ (Sigma-Aldrich, 99+ %) were employed for the electrodeposition of the anode. Distilled water (DI-Water) from Merck Millipore was used to clean samples and contacts of the device. Lithium fluoride LiF (Sigma-Aldrich, 99.99+ %) and hydrochloric acid HCl (Sigma-Aldrich, 37 %) were used to synthesize $Ti_3C_2Tx$ MXenes. 125 μm width Kapton © sheets were used as substrates.

### 2.2. Methods

Electron microscopy imaging was carried out on both the anode and the cathode with a Field-Emission Scanning Electron Microscope (FESEM Supra 40, manufactured by Zeiss).

PANalytical X`Pert MRD Pro-powder diffractometer equipped using the 1D PIXcel detector has been used for the X-ray diffraction analysis (Malvern PANalytical, the United Kingdom) of the anode. The diffractograms were collected in Bragg-Brentano reflection mode by using a Cu K$\alpha_{1/2}$ radiation, at an operating voltage of 40 kV and a tube current of 40 mA. The instrumental broadening was computed by Caglioti-equation based on the reflections of a standard $LaB_6$ powder NIST660a. The measurements were carried out in continuous mode with a step size of 2 θ = 0.0131° and a data time per step of 1500s. QualX equipped with COD database was employed for the qualitative phase determination and MAUD-free software for the quantitative analysis and the refinement. The COD cards matching the diffraction patterns of the manganese oxides are the numbers 1514103 ($\alpha-Mn_2O_3$), 1528293 ($NaMn_2O_4$) and 4002329 ($Na_2Mn_3O_7$).

For the cathode, X-ray diffraction measurements were carried out in the range from 5 to 90° in 2θ-scale with a step size 0.008° and time per step 1 s on a Bruker D8 Advance diffractometer using CuK$\alpha$1 radiation (40 kV, 40 mA) according to the Bragg-Brentano configuration.

Micro-Raman spectroscopy was performed by using a Renishaw InVia Qontor Raman microscope. A laser diode source (λ=532 nm) was used with 5 mW power, and sample inspection occurred through a microscope objective (50X), with a backscattering light collection setup. The Raman spectrum analysis was carried out with Fityk software [51]. Lorentzian functions were used as fitting functions. All the data are reported with baseline correction.

X-ray Photoelectron Spectroscopy (XPS) measurements were carried out by means of a PHI 5000 Versaprobe spectrometer (Physical Electronics, USA), equipped with a monochromatic Al k-alpha source (1486.6 eV), together with a dual beam neutralizer system, composed by an electron beam and an Ar ion source, used to compensate surface charging phenomena. Survey and High Resolution (HR) scans have been exploited to get information related to surface relative chemical composition and elements oxidation states. Data analysis has been performed thanks to Multipak 9.7 version dedicated software, provided by PHI.

The electrochemical measurements were performed with the VMP3 (Biologic, USA) in a 3-electrodes configuration by using an Ag/AgCl reference electrode and a 12 mm diameter carbon based counter electrode fabricated according to our previous work [18], in 1 M $Na_2SO_4$.

The electrochemical measurement involved the Open Circuit Potential (OCP) analysis, followed by an Electrochemical Impedance Spectroscopy (EIS) and cyclic voltammetry (CV).

The samples were left to rest at OCP for 10 min, to stabilize the cell. Then the EIS measurements were carried out between 10 mHz and 1
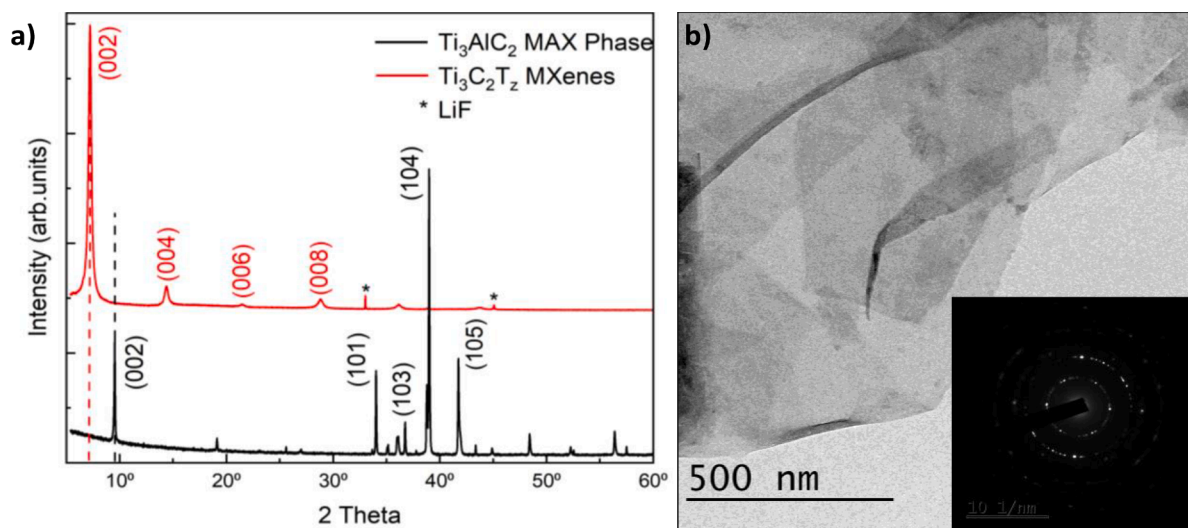
**Fig. 1.** (a) XRD patterns of $Ti_3AlC_2$ MAX phase precursor (black curve) and $Ti_3C_2T_x$ MXenes (red curve); (b) TEM micrograph of $Ti_3C_2T_x$ flakes with corresponding SAED pattern (inset).

MHz. 6 points per decade were sampled, applying a signal of 20 $mV_{pp}$ amplitude. The evaluation of the device electrochemical stability window was performed by means of repeated CV at different increasing polarizations at 5 mV $s^{-1}$ (see Figure S1, Supporting Information). The potential was increased by 0.1 V in anodic direction in the different experiments. Constant current charge/discharge (CCCD) were carried out using Arbin BT2000. After letting the device rest at OCV, charge/discharge was performed at different current densities: 0.5 $mA/cm^2$, 1 $mA/cm^2$, 2 $mA/cm^2$, 5 $mA/cm^2$, 10 $mA/cm^2$, and then again 0.5 $mA/cm^2$. The measurement ends with the same current as the first set in order to see if there is a stabilization of the cell over time. This last type of measurements was used to derive the rate capabilities with respect to different currents, energy density and power density.

### 2.3. Fabrication of laser-induced graphene electrodes

Electrodes were fabricated through laser scribing exploiting the methodology used in our previous works.[18,19,52] Briefly, a laser source of $CO_2$ (EOX 30 W laser, provided by DataLogic) was used to produce LIG onto 125 μm Kapton sheets, to obtain 0.5 × 2 $cm^2$ LIG electrodes. This set of parameters allows the graphenization of the polyimide sheet in a highly porous structure. The electrodes will be covered with titanium, exposing a 0.5 × 0.5 $cm^2$ active area.

### 2.4. Anode: electrodeposition of manganese oxide onto LIG

An aqueous solution containing manganese acetate was employed for the electrodeposition of manganese oxides onto the above mentioned LIG electrodes [53]. The solution was obtained mixing 0.1 M Mn $(CH_3COO)_2$ and 0.1 M $Na_2SO_4$ in DI-water. $Na_2SO_4$ was used as supporting electrolyte.

The electrodeposition of manganese oxides was carried out in a three-electrode system where an Ag/AgCl saturated 3 M KCl was used as reference electrode and the LIG was 2.5 cm apart from a platinum bar used as counter electrode.

In order to deposit the manganese oxide, a constant current of 1 $mA/cm^2$ for 5 up to 60 min was applied by using a potentiosat/galvanostat (Autolab M101 supplied by Metrohm, Netherlands). The gravimetric measurement showed an almost quadratic behaviour of the mass with respect to deposition time, see Figure S2. The electrodes measured in a 3-electrode configuration were the ones obtained within 1 h of deposition.

### 2.5. Cathode: infiltration of MXene into LIG

MXene sheets were obtained by selective chemical etching of $Ti_3AlC_2$ in a mixture of LiF and 9 M HCl. The mixture was kept under continuous stirring at 40 °C for 24 h. After that, the suspension was washed several times with DI water until a neutral pH (6–7) was reached. A suspension of well-delaminated MXene flakes was vacuum filtered and dried. Electrophoretic deposition onto LIG was carried out to accommodate the MXene structures onto the customized current collector without any binding agent.

The dried powder was bell-milled into fine grains (see Figure S3, Supporting Informations). A dispersion of 10 mg/ml of MXene in DI-water saturated with nitrogen was employed for the electrophoretic deposition which was carried by applying a voltage of 15 V between the LIG and a platinum bar.

### 2.6. Asymmetric device

Asymmetric devices were assembled by balancing the capacities [54] of the $MnO_x$-LIG and MXene-LIG electrodes. The device was assembled in a parallel configuration with a 675 μm thick glass fibre (1823–257, Whatman™, UK) used as separator. The active area of the device is 0.25 $cm^2$. The electrolyte was 1 M $Na_2SO_4$ and the devices were assembled in pouch cells with grids of titanium as tabs. The manganese oxide mass was chosen according to the gravimetric curve in order to obtain a charge balancing between the anode and the cathode.

## 3. Results and discussion

Analysis were first performed on the anode and cathode singularly. After that, a charge balancing was performed and a whole device was assembled and tested.

### 3.1. Electrodes characterization

The produced LIG electrodes were exploited as current collectors and as substrates for the final device anode and cathode engineering. Anodes were prepared via anodic deposition of the manganese oxide phase, while cathodes were prepared via electrophoretic deposition of the synthesized MXene. Physical-chemical measurements were carried out on the anode to characterize the deposited TMO. The cathode active material was characterized prior to its deposition. Charge balancing was performed to optimize the device's energy storage capabilities of the
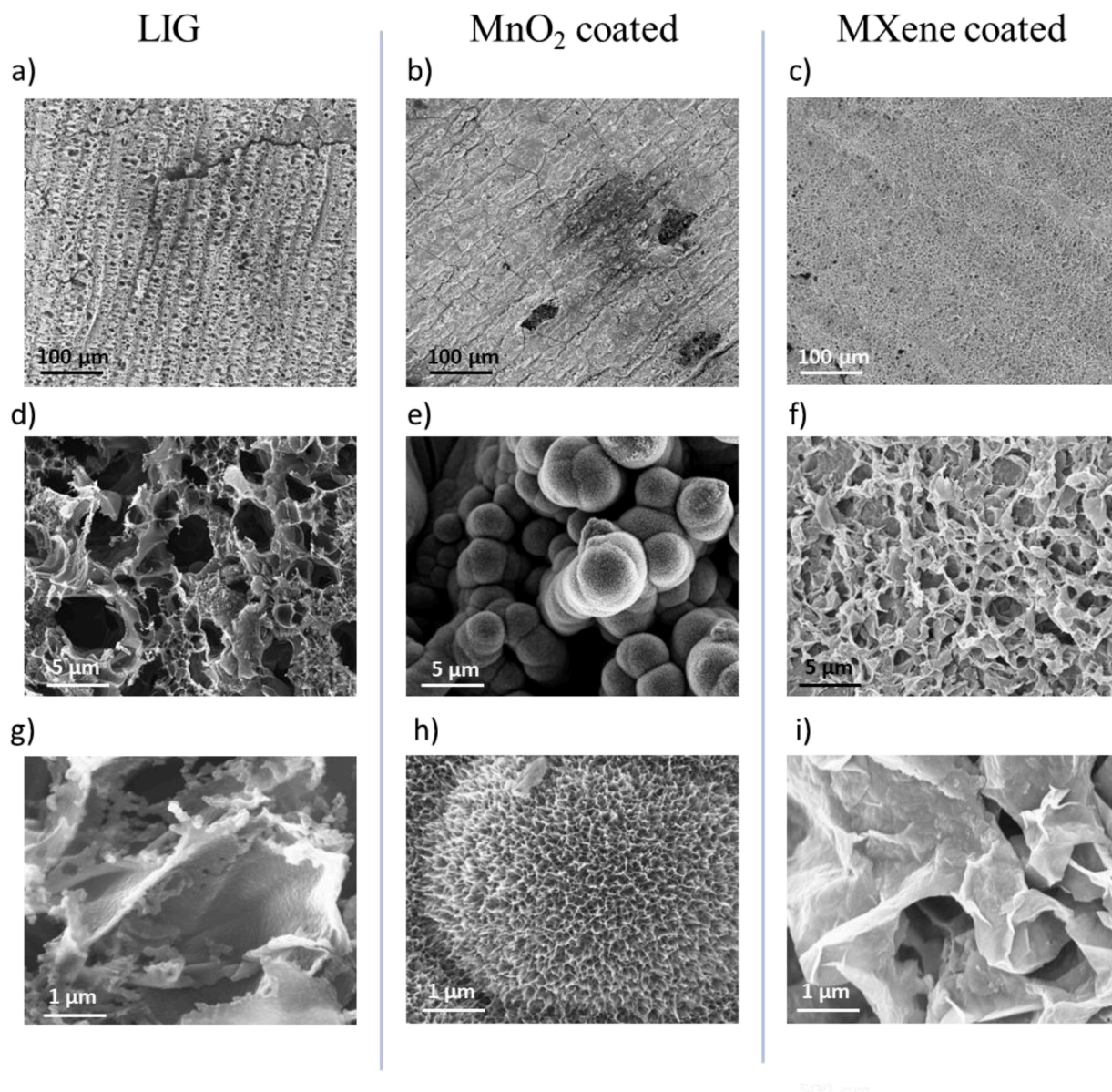
**Fig. 2.** Micrographs acquired by different magnification at FESEM. LIG images are on the left column. In the middle column MnO$_2$ decorated LIG is shown, while in the last column MXene decoration is appreciated. The comparison is proposed at 100 μm scale (a,b,c), 5 μm scale (d,e,f) and 1 μm scale (g–i).

final devices. The balancing was performed through the control of the LIG electrode mass loadings since the LIG current collectors for the anode and cathode were equally shaped. Charge balancing effectiveness was evaluated by means of electrochemical measurements on balanced devices.

The first preliminary characterizations were developed in the MXene sheets directly, involving XRD, TEM and EDX analysis. Results are shown in Fig. 1.

The successful producing of MXenes is confirmed by the absence of Ti$_3$AlC$_2$ peaks in the XRD pattern of the MAX phase after etching (Fig. 1a), red curve). We also observed a clear shift of Ti$_3$AlC$_2$ (002) peak towards lower angles after exfoliation. This is due to the removal of Al from the precursor and the simultaneous intercalation of water and Li-ions occurring during synthesis, which leads to an increase in the c-parameter of the stacked Ti$_3$C$_2$ layers. Analogous to exfoliated graphene, Ti$_3$C$_2$T$_x$ exhibits typical flake features which are illustrated by TEM (Fig. 1b)). The flakes are transparent, irregular in shape and quite large, with an average size of 1–2 μm. The selected area electron diffraction (SAED) pattern of the Ti$_3$C$_2$Tx flakes shows the hexagonal arrangement

of atoms, which retains the symmetry of the parent precursor and confirms the high crystallinity of the produced 2D sheets.

As described in Section 2.5, the as-prepared Ti$_3$C$_2$T$_x$ was dispersed in an aqueous solution and deposited over the LIG current collector via an electrophoretic process. The success of the process was first verified through and FESEM images of the LIG surface. In Fig. 2 it is possible to appreciate the MXene deposition onto the electrode surface. At low magnification, it is shown that electrophoresis led to a homogeneous coverage of the LIG surface. At higher magnification, in Fig. 2f and 2i, it is appreciable that the decoration completely covered the LIG surface. Indeed, the visible macropores cavities present on the LIG sample result in a reduced diameter suggesting a full inclusion of the MXene. Further, the surface features differ between the LIG and the deposited MXene considering Fig. 2c and 2i. Ti$_3$C$_2$T$_x$ has been widely studied in pseudo-capacitive systems for its intercalation pseudocapacitance in either organic or aqueous electrolytes based on Na ions [55,56] as cathode material, therefore, in this work, it will be exploited at the cathode side as described in the following.

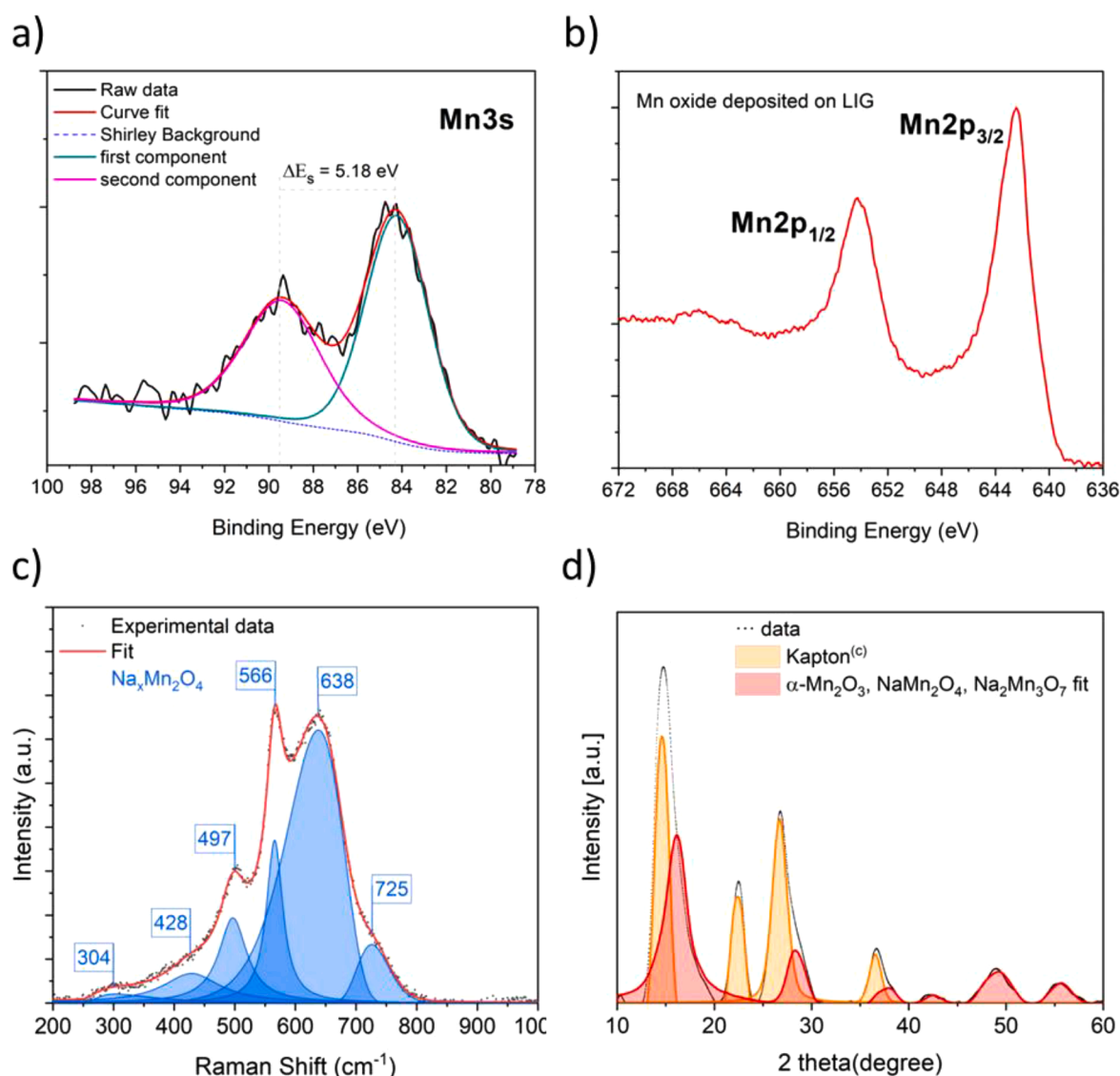Manganese oxides are suitable as anode materials for

**Fig. 3.** (a) XPS HR spectrum of Mn2p and (b) XPS HR spectrum of Mn3s doublet. (c) Raman spectrum (and relative fit) of the manganese oxide deposited onto the LIG support. (d) XRD patterns (and relative fit) of LIG decorated through manganese electrodeposition.

**Table 1**
XRD parameters for $MnO_x$ decorated LIG.

| COD card | | *1,514,103* | *1,528,293* | *4,002,329* |
|---|---|---|---|---|
| **Structure** | | $\alpha$-$Mn_2O_3$ Value | $NaMn_2O_4$ | $Na_2Mn_3O_7$ |
| **Cell [Å]** | *a* | 9.3 | 8.7 | 6.7 |
| | *b* | 9.5 | 1 | 7.1 |
| | *c* | 9.7 | 2.9 | 7.8 |
| **Crystalline size [Å]** | | 99.5 | 207.8 | 67 |
| **Microstrain** | | 0.0019 | 0.0103 | 0.005 |
| **Density [kg/m³]** | | 8.7 | 12.8 | 3.6 |
| **Weight [ %]** | | 3.37 +- 0.0214 | 2.994 | 93.6 +- 0.35 |

supercapacitors. In this work, an anodic electrodeposition process was implemented in a Mn-based salt electrolyte containing Na-based supporting electrolyte. The TMO was deposited on the LIG current collector, as described in Section 2.4. In Fig. 2b it is shown that the whole electrode after deposition develops a homogeneous layer of manganese.

The micrographs show that the LIG electrode has a mesophorous morphology with random shapes and wrinkled flakes that manifest a rough surface (Fig 2a)). The electrodeposition of manganese oxides massively modifies the appearance of the overall surface with a more continuous and compact layer which at higher magnification shows its peculiar shape of spherical aggregates composed by sharp growths (nanometer wide) akin a chestnut burr.

Under the simple term of "manganese oxide" a huge number of compounds of many different phases can be found and the number becomes countless when considering the manganese oxyhydroxide system with stoichiometric alkali metals. The manganese has five oxidation states plus the metallic form. And those multiple valences can be surrounded by several structures when bonded with oxygen. Each one of those presents different electrochemical properties [57] either for electrocatalysis and for storage. Therefore, to unravel the possible deposited phases produced after the electrodeposition, XPS, Raman spectroscopy and XRD analysis were carried out. Mn, as already mentioned, represents a tricky element to be deconvoluted by XPS analysis, due to its numerous oxidation states, together with its multiplet splitting and components overlapping, when more than one oxidation state is present in the compound. For this reason, Mn photoelectron peaks were analysed very carefully, adding the analysis of the secondary peak Mn3s doublet to the main one, Mn2p doublet. From Fig. 3a, at a first glance, we can see that Mn2p doublet do not show the typical
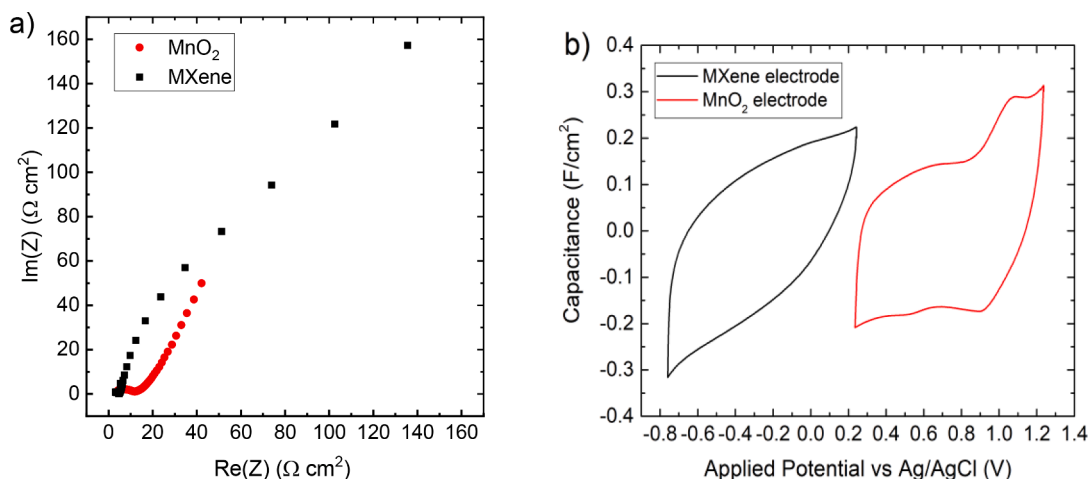
**Fig. 4.** Electrochemical measurements of the two electrodes. (a) EIS between 10 mHz and 1 MHz. (b) Cyclic voltammetries performed at 5 mV $s^{-1}$.

shake-up satellite above 644 eV, which is a fingerprint for Mn(+2) phase [58]. The shape is the one typical for Mn (+3) oxidation state, as reported in the literature [59]. But to be more than confident, the Mn3s doublet was observed and the relative distance between the two peaks ($\Delta$Es) (see Fig. 3b)) was measured. This value (5.18 eV) can be further applied to the formula presented by M. Sun et al.[60] in which is used to obtain the Average Oxidation State (AOS) of the material surface: AOS = 8.95 − 1.13 ● $\Delta$Es (eV). The calculated value is equal to 3.10. This leads to a mean surface oxidation state equal to Mn (+3), as in $Mn_2O_3$ or MnOOH.

In Fig. 3c it is reported the result concerning the Raman characterization of manganese oxide deposited onto the LIG current collector support. According to the XPS results, the only possible Mn oxidation state on the surface is +3. By following this route, we tried to assign a specific phase to the surface layer. The peaks above 600 $cm^{-1}$ are due to the symmetrical stretching vibrations of $MnO_6$ octahedra with different Mn oxidation states (+3 and +4). In the report of Xu et al., they show the electrochemical and chemical-physical characterization of chemically synthesized birnessite manganese oxides, hydrated and Na intercalated, for battery application. In this work, they show the influence of hydration and Na content in the synthesized materials assigning to 638 $cm^{-1}$ wavenumber the molecular vibration of the $Mn^{3+}$ while the evolution of the peak at 566 $cm^{-1}$ wavenumber was attributed to the presence of $Na^+$ cations in the interlayers [41]. The Na+ cation presence can be attributed to a phase stabilization during the electrochemical deposition due to its presence in the deposition bath. According to Julien et al. [61], the position of the characteristic peak of structural octahedra of pristine birnessite phases is shifted depending on the intercalant cation size affecting the interlayer spacing. It is worth noting that the assignment of the peak at 566 $cm^{-1}$ can be attributed to the vibration of the $MnO_6$ octahedra in the pristine birnessite phase as reported in [25]. In the latter report, Julien and co-workers compared their Raman spectrum results with calculated modes according to group theory. Further, shoulders at high wavenumbers above 700 cm-1 were reported for pristine and doped birnessite obtained synthetically via sol-gel method. Discrepancies between group theory calculations and experimental data can be attributed to the defect chemistry and local disorder in the inferred Na-birnessite causing vibrational modes having little to no intensity to be detected. Indeed, the broad peaks are suggesting the presence of a highly disordered material.

In Fig. 3d the X-ray diffraction (XRD) pattern of the LIG-Manganese oxides modified electrode is presented. The diffraction pattern contains a combination of broad peaks that arise from the polyimide substrate (Kapton © in orange), $\alpha$-$Mn_2O_3$ and two sodium-manganese-oxides based structures with peculiar characteristics that were identified as $Na_2Mn_3O_7$ and $NaMn_2O_4$, in accordance with the Raman spectrum and,

while no evidence of the graphitized material has been found.

$Na_2Mn_3O_7$ has a triclinic crystal structure having the space group *P-1* and it is composed of alternating layers of $Mn_3O_7$ 2−slabs and Na-ions along the crystallographic (−1 1 0) direction. Those $Mn_3O_7$ 2−layers are built with the edge-sharing $MnO_6$ octahedra and are well separated (~5.57 Å) by an intermediate Na-ion layer. In each $Mn_3O_7$ 2− layer, 1/7 of the Mn sites are regularly vacant, leading to a maple-leaf lattice geometry of the Mn ions. Within the Na-ion layers, sodium atoms are located at two distinct crystallographic sites with distorted prismatic $Na_1O_5$ (situated above the Mn vacant sites) and distorted octahedral $Na_2O_6$ environments [62]. In the $\alpha$-$Mn_2O_3$ structure, also known as bixbyite, the $Mn^{3+}$ ions are octahedrally coordinated, while the O ions have 4 Mn neighbors. The bixbyite structure can be viewed as a close-packed lattice of Mn with O ions filling 3/4 of the tetrahedral interstitials in a pattern with Ia3 symmetry. Below about 300 K, $\alpha$-$Mn_2O_3$ transforms from cubic to an orthorhombic structure with Pbca symmetry. Experimentally, the lattice parameters ($a,b,c$) saturate at low temperatures to approximately $a = 9.41$ Å, $b = 9.45$ Å, and $c = 9.37$ Å In the cubic bixbyite phase, 24 of 32 Mn atoms exhibit distorted coordination whereas the remaining 8 Mn atoms, which occupy fixed-coordinate high-symmetry positions, retain regular coordination environments. The orthorhombic phase accommodates Jahn-Teller distortion of the remaining 8 octahedra. [63]

In Fig. 3d), the $Na_2Mn_3O_7$, $NaMn_2O_4$ and the $\alpha$-$Mn_3O_3$ XRD patterns were fit. The first intense reflections of the $NaMn_2O_4$ and the $\alpha$-$Mn_2O_3$ are at 18.8 and 16.3 °, respectively, therefore the peak at 2thetas of 16 ° was the footprint to recognize the (1 0 0) plane of $Na_2Mn_3O_7$. The structure refinement allowed to estimate this distance to be of 5.69 Å in the sample. The crystalline dimension of this phase has been estimated to be around 67 Å with a microstrain of 5u Interestingly, the atomic refinement showed that the layered structure is Mn-deficient with a computed stoichiometry of $Na_{2.04}Mn_{2.88}O_7$, therefore with even more Mn vacant sites. This phase represents the 94 % of those recognized. Either the $NaMn_2O_4$ and $\alpha$-$Mn_2O_3$ are the 3 % of the sample with crystal size of 210 and 100 Å on average, respectively. The calculated cell parameters, weight % and density of the phases is reported in Table 1. Such broad peaks in the XRD patterns appear not only for the small crystal sizes, but also for the natural stacking faults of the $Mn_3O_7$ 2−layers in the crystal structure of $Na_2Mn_3O_7$.

Electrochemical measurements were carried out to evaluate the energy storage performance of the electrodes.

A comparison between the performances of the obtained anode and cathode are shown in Fig. 4.

In Fig 4a it is reported the comparison between the EIS of the two electrodes. As it can be appreciated, the MXene electrode reveals a more resistive behaviour if compared to the MnO one.
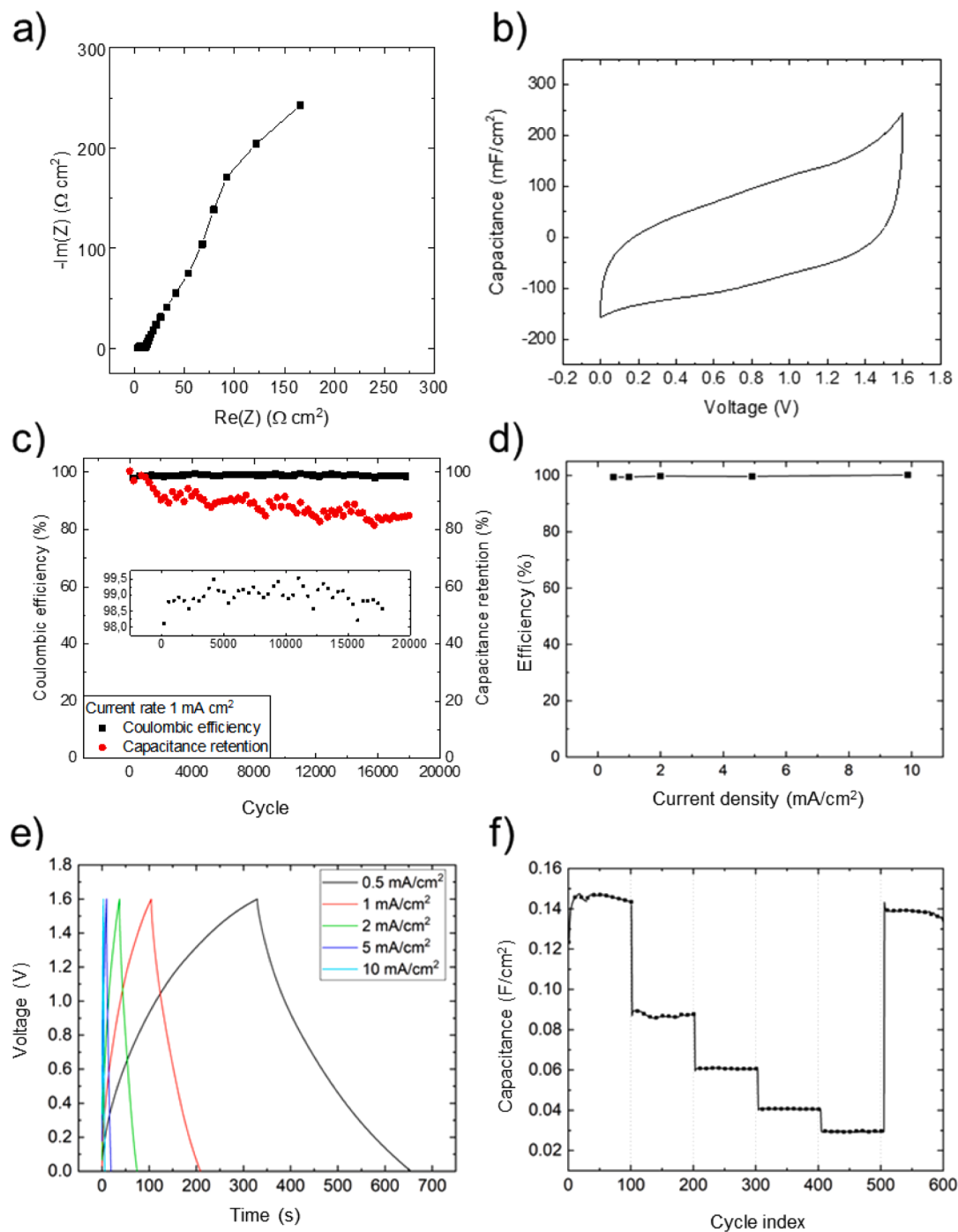
**Fig. 5.** Electrochemical measurements of the device. (a) EIS at OCV=340 mV, frequency [10 m; 1 M] Hz (b) Cyclic voltammetry at 5 mV s$^{-1}$ in a voltage window 1.6 V (c) Coulombic efficiency and capacitance retention calculated from charge/discharge at different cycles. (d) Coulombic efficiency calculated from charge/discharge at different current densities. (e) Voltage profile during CCCD carried out 0.5 mA/cm$^2$, 1 mA/cm$^2$, 2 mA/cm$^2$, 5 mA/cm$^2$, 10 mA/cm$^2$. (f) Capacitance calculated during CCCD.

The electrode decorated with manganese oxides shows an enhancement [18,64] in the supercapacitive behaviour after the deposition. The setup shows 2.25 Ω cm$^2$ equivalent series resistance (ESR). The areal capacitance was retrieved from the cyclic voltammetries. After 100 cycles the bare sample reached 42.3 mF cm$^{-2}$ while the one decorated with manganese oxide reached up to 165.5 mF cm$^{-2}$, meaning a 391 % increase in capacitance by simply depositing the MnO$_2$ on the LIG.

Electrical conductivity has a significant role in intercalation/deintercalation-based energy storage devices where transport of Na$^+$ ions takes place within the electrode materials (either layered Na$_2$Mn$_3$O$_4$, NaMn$_2$O$_4$, α-Mn$_2$O$_3$ and MXene). Consistent drop in storage performance at high charge/discharge rates is due to a slow motion of cations through the material. Various approaches *via* structure modification, introduction of defects, selective doping with transition metal ions, have been proposed [65] to improve the ionic transport, reduce the irreversible hysteresis and the voltage decay. Being the electrical response only provided by the microstructural network, the understanding of the microscopic conduction at the electrode structures is key factor for understanding the electrochemical features and to design of high-performance materials and devices.
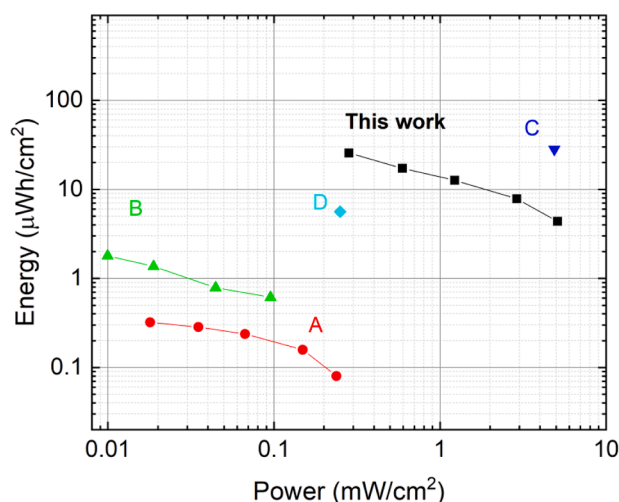
**Fig. 6.** Ragone plot of the device compared with the current state of the art (the references are shown in Table 2).

α-$Mn_2O_3$ is a semiconductor with a high theoretical capacity of 1018 mAh g$^{-1}$ with respect to lithium intercalation at a low operating voltage (nominal voltage 0.7 V) [66]. It is significant in supercapacitor because of its one-electron transfer caused by electrochemical redox activity *via* the $Mn^{3+}$ to $Mn^{4+}$ transition, but its poor electrical conductivity usually limits the solid-state diffusion of charges with a consequent reduction of the power density. $NaMn_2O_4$ has been employed for Na-ion batteries because of its theoretical specific capacity ~136 mAh/g. The discharge profile shows the transition from the usual plateau to linear decay profile typical of extrinsic pseudocapacitors when the crystalline dimension lowers from highly crystalline micro-rods [67]to nano-sized particles of 8–10 nm [68] in standard battery-electrolytes (1 M $NaClO_4$ solution in EC:DMC solvent). $Na_2Mn_3O_7$ in virtue of the intermediate layers of Na-ions alone, shows either a high electric and ionic conductivity, high energy density, low dissipation energy, and anisotropic nature [69]. Being layered, there is a reasonable degree of freedom in their crystal structure to expand the interstitial space between layers to provide better insertion of $Na^+$ ions among the lamellas.

Recently, $Na_2Mn_3O_7$ with its layered structure has been reported as an efficient material for batteries with great electrochemical reversibility (<50 mV), high energy storage capacity, and high structural stability [70]: it has been proven that one (of three) oxygen 2p orbitals is nearly unhybridized in the Na−O−Na configuration in the layered Na-transition metal oxide due to the very strong ionic nature of the Na−O bonds. Thus, during the fully charged state of the cathode in which the large amounts of interlayer $Na^+$ are removed, $Na^+$ ions on the transition metal layer can be replaced by vacancies and they decrease the degree of orbital overlapping. Therefore, a narrower nonbonding oxygen 2p states is created in the vacancy-rich layer (those of Na-O-Na) in both charged and discharged states [71].

It has been assumed for long times that creating large amounts of vacancies on the transition metal layers is generally believed to be a thermodynamically unfavourable process, but few natural phyllomanganite minerals have been reported to possess appreciable amounts of Mn vacancies and even several vacancy-rich sodium or copper

analogues of the mineral chalcophanite can be synthesized via soft methods at relatively low temperatures [72]. The transition metal vacancies induced by the lattice oxygen redox activity of this family of compounds were supposed to be one of the phenomena contributing to the charge storage of such materials. In the case of $Na_2Mn_3O_7$, it has been observed that the voltage hysteresis is even smaller than in other oxygen-redox capacitive materials [38] modifying therefore the older assumption and opening the idea to propose the transition metal vacancies induced by the lattice oxygen redox activity of this family of compounds one of the phenomena contributing to the charge storage of such materials.

Further studies have shown that upon introduction of Mn vacancies in $Na_2Mn_3O_7$, the specific capacity can be enhanced up to 220 mAh g$^{-1}$ in Na-ion battery electrolyte[75], while in aqueous Zn ion battery a capacity of 245 mAh g$^{-1}$ is associated to the nominal voltage of 1.5 V . [74] Equally of great importance, density functional theory (DFT) calculations showed that under working conditions, the crystal structure of $Na_2Mn_3O_7$ remains stable and that the migration barrier of the sodium was so low (~0.18 eV) to ensure good ionic conductivity, good rate capability and that he entire conductance was mediated by Na-ions alone with no migration of the $Mn^{4+}$ perpendicular to the layers [73, 75]. In the LIG-modified manganese oxide sample, the $Na_2Mn_3O_7$ is slightly deficient in Mn, generating more vacancies that are presumed to increase the electrical conductivity and the Na mobility. Being the LIG current collector graphitized and being measured by XPS the presence of $Mn^{3+}$ on the very surface, we hypnotize a continuous formation of layers form the graphene-like structure of the LIG to the $Na_2Mn_3O_4$ onto which $NaMn_2O_4$, and α-$Mn_2O_3$ grow with crystallites of tens of nm which give rise to such large ESA shown in the red voltammetry of Fig. 4.

### 3.2. Device characterization

After the device was sealed in the pouch cell, electrochemical tests were carried out.

The device has an active area of 0.25 cm$^2$, and the employed electrolyte is $Na_2SO_4$ 1M

In Fig. 5a it is reported the EIS spectrum of the assembled device. The open circuit voltage of the cell is 340 mV. The device ESR is 4 Ω cm$^2$. The semicircle at high frequencies can be attributed to a charge transfer resistance of the manganese decorated electrode as suggested by the spectroscopies of Fig. 4a. The low frequency resistive behavior is attributed to MXene electrode.

In Fig. 5b, the device CV is reported showing a resistive behaviour. The CV shows the typical features of a SC and good stability at the rated voltage of 1.6 V.

Fig. 5c–f report the results of the galvanostatic tests. Fig. 5c reports the evolution of the coulombic efficiency while cycling the device for 180,000 cycles at 1 mA/cm$^2$. The coulombic efficiency stabilises around 99 % after 600 cycles of charge discharge up to 180,000, which corresponds to 41 days of measurement. Varying the current density between 0.5 mA/cm$^2$ and 10 mA cm$^{-2}$ the coulombic efficiency is always above 98 %, as it can be appreciated in Fig. 5d. The galvanostatic profiles are reported in Fig. 5e). The almost linear charge and discharge profiles are typical of capacitive systems, confirming the pseudocapacitive behavior of the device. The linearity is less evident for low currents, because the leakage currents become not negligible with respect to the charging

**Table 2**
Power and energy comparison between the current state of the art.

| | Electrode | Electrolyte | Energy (μWh cm$^{-2}$) | Power (mW cm$^{-2}$) | Refs. |
|---|---|---|---|---|---|
| This work | LIG + MnO$_2$/MXene | Na$_2$SO$_4$ 1M | 25.57 | 5.1 | / |
| A | LIG | KCl 1M | 2 | 0.23 | [18] |
| B | LIG | 1-Butyl-1-methylpyrrolidinium bis(trifluoromethanesulfonyl)imide | 4.5 | 0.9 | [76] |
| C | Carbon Fabric + MnO$_2$/MXene | Na$_2$SO$_4$ 1M | 4.87 | 28,16 | [21] |
| D | Nitrogen-Boron codoped LIG | PVA–H$_2$SO$_4$ | 5.61 | 0.025 | [77] |

ones. The capacity retention evaluated during the CCCD test is reported in Fig. 5e), The device starts from an average capacitance of 123.6 mF cm$^{-2}$ at the lower current rate. Increasing the current rate drastically lowers the retained capacitance due to the resistive behaviour of the device. However, as suggested by the last 100 cycles of Fig. 5f, the device recovers its initial capacitance after cycling, stabilizing at 136 mF cm$^{-2}$.

Power and energy densities were evaluated from the CCCD test and reported in the Ragone plot of Fig. 6. The device rated 25.57 μWh cm$^{-2}$ at a relatively low power density of 0.28 mW cm$^{-2}$. By increasing the power density up to 5.1 mW cm$^{-2}$, the energy density is reduced to 4.36 μWh cm$^{-2}$. This variation can be attributed by the dissipative properties of the device. However, if compared to literature, the device shows remarkable features. Some references involve LIG electrodes as current collector, decorated or enhanced with chemical treatments, while some references are the those for electrodes decorated with MXene and manganese oxide, but without LIG. From the Ragone plot it is worth noticing that the presented devices are in line with the current state-of-the-art. Data reported in the Ragone plot are shown in Table 2, where it is possible to compare power, energy, capacitance and the information on the electrodes and the electrolytes are listed.

The electrodeposition of MXene and MnOx led to higher energy and power densities compared to other improvements developed for the LIG substrate (see Table 2, ref. A, B, D). Decoration of MXene and manganese on LIG led also to higher performances with respect to electrodeposition carbon fabric (see Table 2, ref. C).

## 4. Conclusion

In conclusion, this work reports on the fabrication of an asymmetric flexible micro-supercapacitor with remarkable energy storage performance. The device was assembled by exploiting LIG as current collector. The active materials were deposited by means of electrochemical processes such as electrophoresis for the deposition of MXene and plating for the deposition of a manganese oxide phase. The physical-chemical characterization of the manganese oxide revealed the plausible formation of a sodium compensated birnessite phase.

Onto the manganese oxide-LIG electrode, Raman, X-ray photoelectron spectroscopy and XRD refinement demonstrate that the charge compensation is dominated by the oxygen redox reaction and Mn$^{3+}$/Mn$^{4+}$ redox reaction separately. These phenomena led to a strong improvement in the anode performances, providing an anode with an areal capacitance of 165.5 mF cm$^{-2}$. MXene electrophoresis on the counter electrode led to a reduction of overall resistance and an improvement in the charge storage up to 133.82 mF cm$^{-2}$.

The assembled device was able to work up to 1.6 V with a total capacitance of 136 mF cm$^{-2}$. The supercapacitor was also stable in time, keeping an efficiency of 99.6 % after 600 constant current charge/discharge cycles. Energy and power densities were 25.57 μWh cm$^{-2}$ and 5.1 mW cm$^{-2}$, respectively. Finally, the potential window has been extended with respect to the classic aqueous based devices.

## CRediT authorship contribution statement

**Marco Reina:** Methodology, Formal analysis, Investigation, Data curation, Writing – original draft, Writing – review & editing, Visualization. **Mara Serrapede:** Formal analysis, Investigation, Data curation, Writing – original draft. **Pietro Zaccagnini:** Methodology, Formal analysis, Investigation, Data curation, Writing – original draft, Supervision. **Alessandro Pedico:** Investigation, Data curation, Writing – original draft. **Micaela Castellino:** Formal analysis, Investigation, Data curation, Writing – original draft. **Stefano Bianco:** Investigation, Formal analysis. **Thierry Ouisse:** Resources, Formal analysis, Investigation, Data curation. **Hanna Pazniak:** Resources, Formal analysis, Investigation, Data curation, Writing – original draft. **Jesus Gonzalez-Julian:** Resources, Formal analysis, Investigation. **Andrea Lamberti:** Conceptualization, Resources, Supervision, Project administration, Funding acquisition.

## Declaration of Competing Interest

The authors declare the following financial interests/personal relationships which may be considered as potential competing interests: Marco Reina reports financial support was provided by ERC and by PNRR.

## Data availability

Data will be made available on request.

## Aknowledgements

## Supplementary materials

Supplementary material associated with this article can be found, in the online version, at doi:10.1016/j.electacta.2023.143163.

## Bibliography

[1] S. Wang, J. Ma, X. Shi, Y. Zhu, Z.S. Wu, Recent status and future perspectives of ultracompact and customizable micro-supercapacitors, Nano Res. Energy 1 (2022), e9120018, https://doi.org/10.26599/NRE.2022.9120018.

[2] Y. Zhu, S. Wang, J. Ma, P. Das, S. Zheng, Z.S. Wu, Recent status and future perspectives of 2D MXene for micro-supercapacitors and micro-batteries, Energy Storage Mater. 51 (2022) 500–526, https://doi.org/10.1016/j.ensm.2022.06.044.

[3] W.M. Zhao, J.D. Shen, X.J. Xu, W.X. He, L. Liu, Z.H. Chen, J. Liu, Functional catalysts for polysulfide conversion in Li–S batteries: from micro/nanoscale to single atom, Rare Metals 41 (2022) 1080–1100, https://doi.org/10.1007/s12598-021-01865-3.

[4] X. Li, X. Wang, G. Liu, X. Sui, Q. Wu, X. Wang, X. Lv, E. Xie, Z. Zhang, 2.5V "water in salt" aqueous micro-supercapacitors based on polypyrrole-coated NiCo layered double hydroxides, Chem. Eng. J. 452 (2023), 139140, https://doi.org/10.1016/j.cej.2022.139140.

[5] J. Ma, S. Zheng, Y. Cao, Y. Zhu, P. Das, H. Wang, Y. Liu, J. Wang, L. Chi, S. (Frank) Liu, Z. Wu, Aqueous MXene/PH1000 hybrid inks for inkjet-printing micro-supercapacitors with unprecedented volumetric capacitance and modular self-powered microelectronics, Adv. Energy Mater. 11 (2021), 2100746, https://doi.org/10.1002/aenm.202100746.

[6] Z. Cao, J. Fu, M. Wu, T. Hua, H. Hu, Synchronously manipulating Zn$^{2+}$ transfer and hydrogen/oxygen evolution kinetics in MXene host electrodes toward symmetric Zn-ions micro-supercapacitor with enhanced areal energy density, Energy Storage Mater. 40 (2021) 10–21, https://doi.org/10.1016/j.ensm.2021.04.047.

[7] W. Zuo, R. Li, C. Zhou, Y. Li, J. Xia, J. Liu, Battery-supercapacitor hybrid devices: recent progress and future prospects, Adv. Sci. 4 (2017), 1600539, https://doi.org/10.1002/advs.201600539.

[8] G.Z. Chen, Linear and non-linear pseudocapacitances with or without diffusion control, Progr. Natural Sci. Mater. Int. 31 (2021) 792–800, https://doi.org/10.1016/j.pnsc.2021.10.011.

[9] T.-C. Liu, W.G. Pell, B.E. Conway, S.L. Roberson, Behavior of molybdenum nitrides as materials for electrochemical capacitors: comparison with ruthenium oxide, J Electrochem. Soc. 145 (1998) 1882–1888, https://doi.org/10.1149/1.1838571.

[10] X. Wu, H. Yang, M. Yu, J. Liu, S. Li, Design principles of high-voltage aqueous supercapacitors, Mater. Today Energy 21 (2021), 100739, https://doi.org/10.1016/j.mtener.2021.100739.

[11] P. Zaccagnini, A. Lamberti, A perspective on laser-induced graphene for micro-supercapacitor application, Appl. Phys. Lett. 120 (2022), 100501, https://doi.org/10.1063/5.0078707.

[12] S. TRASATTI, Electrochemistry and environment: the role of electrocatalysis*1, Int. J. Hydrogen Energy 20 (1995) 835–844, https://doi.org/10.1016/0360-3199(95)00014-5.

[13] L. Cheng, W. Guo, X. Cao, Y. Dou, L. Huang, Y. Song, J. Su, Z. Zeng, R. Ye, Laser-induced graphene for environmental applications: progress and opportunities, Mater. Chem. Front. 5 (2021) 4874–4891, https://doi.org/10.1039/D1QM00437A.

[14] Y. Xu, Q. Fei, M. Page, G. Zhao, Y. Ling, D. Chen, Z. Yan, Laser-induced graphene for bioelectronics and soft actuators, Nano Res. 14 (2021) 3033–3050, https://doi.org/10.1007/s12274-021-3441-9.

[15] E. Alhajji, F. Zhang, H.N. Alshareef, Status and prospects of laser-induced graphene for battery applications, Energy Technol. 9 (2021), 2100454, https://doi.org/10.1002/ente.202100454.

[16] F.M. Vivaldi, A. Dallinger, A. Bonini, N. Poma, L. Sembranti, D. Biagini, P. Salvo, F. Greco, F. di Francesco, Three-dimensional (3D) laser-induced graphene: structure, properties, and application to chemical sensing, ACS Appl. Mater Interfaces 13 (2021) 30245–30260, https://doi.org/10.1021/acsami.1c05614.

[17] J. Lin, Z. Peng, Y. Liu, F. Ruiz-Zepeda, R. Ye, E.L.G. Samuel, M.J. Yacaman, B. I. Yakobson, J.M. Tour, Laser-induced porous graphene films from commercial polymers, Nat. Commun. 5 (2014) 5714, https://doi.org/10.1038/ncomms6714.

[18] M. Reina, A. Scalia, G. Auxilia, M. Fontana, F. Bella, S. Ferrero, A. Lamberti, Boosting electric double layer capacitance in laser-induced graphene-based supercapacitors, Adv Sustain Syst. 6 (2022), 2100228, https://doi.org/10.1002/adsu.202100228.

[19] F. Clerici, M. Fontana, S. Bianco, M. Serrapede, F. Perrucci, S. Ferrero, E. Tresso, A. Lamberti, *In situ* MoS2 decoration of laser-induced graphene as flexible supercapacitor electrodes, ACS Appl. Mater. Interfaces 8 (2016) 10459–10465, https://doi.org/10.1021/acsami.6b00808.

[20] Y. Wei, W. Luo, X. Li, Z. Lin, C. Hou, M. Ma, J. Ding, T. Li, Y. Ma, PANI-MnO2 and Ti3C2Tx (MXene) as electrodes for high-performance flexible asymmetric supercapacitors, Electrochim. Acta 406 (2022), 139874, https://doi.org/10.1016/j.electacta.2022.139874.

[21] Y. Wei, W. Zheng, W. Luo, B. Dai, J. Ren, M. Ma, T. Li, Y. Ma, All pseudocapacitive MXene-MnO2 flexible asymmetric supercapacitor, J. Energy Storage 45 (2022), 103715, https://doi.org/10.1016/j.est.2021.103715.

[22] A. Rafique, A. Massa, M. Fontana, S. Bianco, A. Chiodoni, C.F. Pirri, S. Hernández, A. Lamberti, Highly uniform anodically deposited film of MnO2 nanoflakes on carbon fibers for flexible and wearable fiber-shaped supercapacitors, ACS Appl. Mater Interfaces 9 (2017) 28386–28393, https://doi.org/10.1021/acsami.7b06311.

[23] M. Serrapede, A. Rafique, M. Fontana, A. Zine, P. Rivolo, S. Bianco, L. Chetibi, E. Tresso, A. Lamberti, Fiber-shaped asymmetric supercapacitor exploiting rGO/Fe2O3 aerogel and electrodeposited MnOx nanosheets on carbon fibers, Carbon N Y 144 (2019) 91–100, https://doi.org/10.1016/j.carbon.2018.12.002.

[24] A. Rafique, U. Zubair, M. Serrapede, M. Fontana, S. Bianco, P. Rivolo, C.F. Pirri, A. Lamberti, Binder free and flexible asymmetric supercapacitor exploiting Mn3O4 and MoS2 nanoflakes on carbon fibers, Nanomaterials 10 (2020) 1084, https://doi.org/10.3390/nano10061084.

[25] Y. Xin, H. Cao, C. Liu, J. Chen, P. Liu, Y. Lu, Z. Ling, A systematic spectroscopic study of laboratory synthesized manganese oxides relevant to Mars, J. Raman Spectrosc. 53 (2022) 340–355, https://doi.org/10.1002/jrs.6231.

[26] L.M. Garten, P. Selvarasu, J. Perkins, D. Ginley, A. Zakutayev, Phase formation of manganese oxide thin films using pulsed laser deposition, Mater Adv. 2 (2021) 303–309, https://doi.org/10.1039/D0MA00417K.

[27] L. Wang, G. Duan, S.M. Chen, X. Liu, Hydrothermally controlled synthesis of α-MnO2, γ-MnOOH, and Mn3O4 nanomaterials with enhanced electrochemical properties, J. Alloys Compd. 752 (2018) 123–132, https://doi.org/10.1016/j.jallcom.2018.03.244.

[28] J. Yin, E.S. Takeuchi, K.J. Takeuchi, A.C. Marschilok, Synthetic control of manganese birnessite: impact of crystallite size on Li, Na, and Mg based electrochemistry, Inorganica Chim. Acta 453 (2016) 230–237, https://doi.org/10.1016/j.ica.2016.08.026.

[29] S. Cheng, L. Yang, D. Chen, X. Ji, Z. Jiang, D. Ding, M. Liu, Phase evolution of an alpha MnO2 -based electrode for pseudo-capacitors probed by in operando Raman spectroscopy, Nano Energy 9 (2014) 161–167, https://doi.org/10.1016/j.nanoen.2014.07.008.

[30] H.Y. Lee, J.B. Goodenough, Supercapacitor behavior with KCl electrolyte, J. Solid State Chem. 144 (1999) 220–223, https://doi.org/10.1006/jssc.1998.8128.

[31] M. Toupin, T. Brousse, D. Bélanger, Charge storage mechanism of MnO2 electrode used in aqueous electrochemical capacitor, Chem. Mater. 16 (2004) 3184–3190, https://doi.org/10.1021/cm049649j.

[32] P. Simon, Y. Gogotsi, Materials for electrochemical capacitors, Nat. Mater. 7 (2008) 845–854, https://doi.org/10.1038/nmat2297.

[33] L. Li, J. Zhang, Z. Peng, Y. Li, C. Gao, Y. Ji, R. Ye, N.D. Kim, Q. Zhong, Y. Yang, H. Fei, G. Ruan, J.M. Tour, High-performance pseudocapacitive microsupercapacitors from laser-induced graphene, Adv. Mater. 28 (2016) 838–845, https://doi.org/10.1002/adma.201503333.

[34] G.X. Li, P.X. Hou, J. Luan, J.C. Li, X. Li, H. Wang, C. Shi, C. Liu, H.M. Cheng, A MnO2 nanosheet/single-wall carbon nanotube hybrid fiber for wearable solid-state supercapacitors, Carbon NY 140 (2018) 634–643, https://doi.org/10.1016/j.carbon.2018.09.011.

[35] T. Guillemin, C. Douard, K. Robert, B. Asbani, C. Lethien, T. Brousse, J. le Bideau, Solid-state 3D micro-supercapacitors based on ionogel electrolyte: influence of adding lithium and sodium salts to the ionic liquid, Energy Storage Mater. 50 (2022) 606–617, https://doi.org/10.1016/j.ensm.2022.05.041.

[36] H.A. Mosqueda, O. Crosnier, L. Athouël, Y. Dandeville, Y. Scudeller, Ph. Guillemet, D.M. Schleich, T. Brousse, Electrolytes for hybrid carbon–MnO2 electrochemical capacitors, Electrochim. Acta 55 (2010) 7479–7483, https://doi.org/10.1016/j.electacta.2010.01.022.

[37] S. Fleischmann, J.B. Mitchell, R. Wang, C. Zhan, D. Jiang, V. Presser, V. Augustyn, Pseudocapacitance: from fundamental understanding to high power energy storage materials, Chem. Rev. 120 (2020) 6738–6782, https://doi.org/10.1021/acs.chemrev.0c00170.

[38] B. Mortemard de Boisse, S. Nishimura, E. Watanabe, L. Lander, A. Tsuchimoto, J. Kikkawa, E. Kobayashi, D. Asakura, M. Okubo, A. Yamada, Highly reversible oxygen-redox chemistry at 4.1V in Na 4/7− x (☐ 1/7 Mn 6/7)O 2 (☐: mn Vacancy), Adv. Energy Mater. 8 (2018), 1800409, https://doi.org/10.1002/aenm.201800409.

[39] Y.H. Son, P.T.M. Bui, H.R. Lee, M.S. Akhtar, D.K. Shah, O.B. Yang, A rapid synthesis of mesoporous Mn2O3 nanoparticles for supercapacitor applications, Coatings 9 (2019) 631, https://doi.org/10.3390/coatings9100631.

[40] E. Adamczyk, V. Pralong, Na2Mn3O7 : a suitable electrode material for Na-ion batteries? Chem. Mater. 29 (2017) 4645–4648, https://doi.org/10.1021/acs.chemmater.7b01390.

[41] Y. Xu, J. Zhu, J. Feng, Y. Wang, X. Wu, P. Ma, X. Zhang, G. Wang, X. Yan, A rechargeable aqueous zinc/sodium manganese oxides battery with robust performance enabled by Na2SO4 electrolyte additive, Energy Storage Mater. 38 (2021) 299–308, https://doi.org/10.1016/j.ensm.2021.03.019.

[42] M. Naguib, O. Mashtalir, J. Carle, V. Presser, J. Lu, L. Hultman, Y. Gogotsi, M. W. Barsoum, Two-dimensional transition metal carbides, ACS Nano 6 (2012) 1322–1331, https://doi.org/10.1021/nn204153h.

[43] M. Naguib, V.N. Mochalin, M.W. Barsoum, Y. Gogotsi, 25th anniversary article: mxenes: a new family of two-dimensional materials, Adv. Mater. 26 (2014) 992–1005, https://doi.org/10.1002/adma.201304138.

[44] M.R. Lukatskaya, S. Kota, Z. Lin, M.Q. Zhao, N. Shpigel, M.D. Levi, J. Halim, P. L. Taberna, M.W. Barsoum, P. Simon, Y. Gogotsi, Ultra-high-rate pseudocapacitive energy storage in two-dimensional transition metal carbides, Nat. Energy 2 (2017) 17105, https://doi.org/10.1038/nenergy.2017.105.

[45] Y. Ando, M. Okubo, A. Yamada, M. Otani, Capacitive versus pseudocapacitive storage in MXene, Adv. Funct. Mater. 30 (2020), 2000820, https://doi.org/10.1002/adfm.202000820.

[46] L. Li, W. Liu, K. Jiang, D. Chen, F. Qu, G. Shen, *In-situ* annealed Ti3C2Tx MXene based all-solid-state flexible Zn-ion hybrid micro supercapacitor array with enhanced stability, Nanomicro Lett. 13 (2021) 100, https://doi.org/10.1007/s40820-021-00634-2.

[47] B. Anasori, M.R. Lukatskaya, Y. Gogotsi, 2D metal carbides and nitrides (MXenes) for energy storage, Nat. Rev. Mater. 2 (2017) 16098, https://doi.org/10.1038/natrevmats.2016.98.

[48] S. Kumar, M.A. Rehman, S. Lee, M. Kim, H. Hong, J.Y. Park, Y. Seo, Supercapacitors based on Ti3C2Tx MXene extracted from supernatant and current collectors passivated by CVD-graphene, Sci. Rep. 11 (2021) 649, https://doi.org/10.1038/s41598-020-80799-9.

[49] N.A. Kyeremateng, T. Brousse, D. Pech, Microsupercapacitors as miniaturized energy-storage components for on-chip electronics, Nat. Nanotechnol. 12 (2017) 7–15, https://doi.org/10.1038/nnano.2016.196.

[50] C. Lethien, J. le Bideau, T. Brousse, Challenges and prospects of 3D micro-supercapacitors for powering the internet of things, Energy Environ. Sci. 12 (2019) 96–115, https://doi.org/10.1039/C8EE02029A.

[51] M. Wojdyr, *Fityk* : a general-purpose peak fitting program, J Appl Crystallogr 43 (2010) 1126–1128, https://doi.org/10.1107/S0021889810030499.

[52] A. Lamberti, F. Clerici, M. Fontana, L. Scaltrito, A Highly stretchable supercapacitor using laser-induced graphene electrodes onto elastomeric substrate, Adv. Energy Mater. 6 (2016), 1600050, https://doi.org/10.1002/aenm.201600050.

[53] Z. Zeng, H. Zhou, X. Long, E. Guo, X. Wang, Electrodeposition of hierarchical manganese oxide on metal nanoparticles decorated nanoporous gold with enhanced supercapacitor performance, J. Alloys Compd. 632 (2015) 376–385, https://doi.org/10.1016/j.jallcom.2015.01.240.

[54] W. Zhao, L. Wei, Q. Fu, X. Guo, High-performance, flexible, solid-state micro-supercapacitors based on printed asymmetric interdigital electrodes and bio-hydrogel for on-chip electronics, J. Power Sources 422 (2019) 73–83, https://doi.org/10.1016/J.JPOWSOUR.2019.03.021.

[55] P. Srimuk, F. Kaasik, B. Krüner, A. Tolosa, S. Fleischmann, N. Jäckel, M.C. Tekeli, M. Aslan, M.E. Suss, V. Presser, MXene as a novel intercalation-type pseudocapacitive cathode and anode for capacitive deionization, J. Mater Chem. A Mater. 4 (2016) 18265–18271, https://doi.org/10.1039/C6TA07833H.

[56] X. Wang, S. Kajiyama, H. Iinuma, E. Hosono, S. Oro, I. Moriguchi, M. Okubo, A. Yamada, Pseudocapacitance of MXene nanosheets for high-power sodium-ion hybrid capacitors, Nat. Commun. 6 (2015) 6544, https://doi.org/10.1038/ncomms7544.

[57] M. Augustin, D. Fenske, I. Bardenhagen, A. Westphal, M. Knipper, T. Plaggenborg, J. Kolny-Olesiak, J. Parisi, Manganese oxide phases and morphologies: a study on calcination temperature and atmospheric dependence, Beilstein J. Nanotechnol. 6 (2015) 47–59, https://doi.org/10.3762/bjnano.6.6.

[58] M.C. Biesinger, B.P. Payne, A.P. Grosvenor, L.W.M. Lau, A.R. Gerson, R.St. C. Smart, Resolving surface chemical states in XPS analysis of first row transition metals, oxides and hydroxides: Cr, Mn, Fe, Co and Ni, Appl. Surf. Sci. 257 (2011) 2717–2730, https://doi.org/10.1016/j.apsusc.2010.10.051.

[59] G. Yang, W. Yan, J. Wang, H. Yang, Fabrication and formation mechanism of Mn2O3 hollow nanofibers by single-spinneret electrospinning, CrystEngComm 16 (2014) 6907–6913, https://doi.org/10.1039/C4CE00521J.

[60] M. Sun, B. Lan, T. Lin, G. Cheng, F. Ye, L. Yu, X. Cheng, X. Zheng, Controlled synthesis of nanostructured manganese oxide: crystalline evolution and catalytic activities, CrystEngComm 15 (2013) 7010, https://doi.org/10.1039/c3ce40603b.

[61] C. Julien, Raman spectra of birnessite manganese dioxides, Solid State Ion. 159 (2003) 345–356, https://doi.org/10.1016/S0167-2738(03)00035-3.

[62] E.A. Raekelboom, A.L. Hector, J. Owen, G. Vitins, M.T. Weller, Syntheses, structures, and preliminary electrochemistry of the layered lithium and sodium manganese(IV) oxides, A2Mn3O7, Chem. Mater. 13 (2001) 4618–4623, https://doi.org/10.1021/cm011105j.

[63] E. Cockayne, I. Levin, H. Wu, A. Llobet, Magnetic structure of bixbyite α-Mn$_2$O$_3$: a combined DFT +$U$ and neutron diffraction study, Phys. Rev. B 87 (2013), 184413, https://doi.org/10.1103/PhysRevB.87.184413.

[64] A. Lamberti, F. Perrucci, M. Caprioli, M. Serrapede, M. Fontana, S. Bianco, S. Ferrero, E. Tresso, New insights on laser-induced graphene electrodes for flexible supercapacitors: tunable morphology and physical properties, Nanotechnology 28 (2017), 174002, https://doi.org/10.1088/1361-6528/aa6615.

[65] K. Vijaya Babu, L. Seeta Devi, V. Veeraiah, K. Anand, Structural and dielectric studies of LiNiPO$_4$ and LiNi$_{0.5}$Co$_{0.5}$PO$_4$ cathode materials for lithium-ion batteries, J. Asian Ceramic Soc. 4 (2016) 269–276, https://doi.org/10.1016/j.jascer.2016.05.001.

[66] Y. Qiu, G.L. Xu, K. Yan, H. Sun, J. Xiao, S. Yang, S.G. Sun, L. Jin, H. Deng, Morphology-conserved transformation: synthesis of hierarchical mesoporous nanostructures of Mn$_2$O$_3$ and the nanostructural effects on Li-ion insertion/deinsertion properties, J. Mater. Chem. 21 (2011) 6346, https://doi.org/10.1039/c1jm00011j.

[67] X. Liu, X. Wang, A. Iyo, H. Yu, D. Li, H. Zhou, High stable post-spinel NaMn$_2$O$_4$ cathode of sodium ion battery, J. Mater. Chem. A 2 (2014) 14822–14826, https://doi.org/10.1039/C4TA03349C.

[68] M.K. Datta, R. Kuruba, P.H. Jampani, S.J. Chung, P. Saha, R. Epur, K. Kadakia, P. Patel, B. Gattu, A. Manivannan, P.N. Kumta, Electrochemical properties of a new nanocrystalline NaMn$_2$O$_4$ cathode for rechargeable sodium ion batteries, Mater. Sci. Eng. B 188 (2014) 1–7, https://doi.org/10.1016/j.mseb.2014.05.007.

[69] M.H. Han, E. Gonzalo, G. Singh, T. Rojo, A comprehensive review of sodium layered oxides: powerful cathodes for Na-ion batteries, Energy Environ Sci. 8 (2015) 81–102, https://doi.org/10.1039/C4EE03192J.

[70] B.C. Saha, A.K. Bera, S.M. Yusuf, Mechanism of Na-Ion conduction in the highly efficient layered battery material Na$_2$Mn$_3$O$_7$, ACS Appl. Energy Mater. 4 (2021) 6040–6054, https://doi.org/10.1021/acsaem.1c00825.

[71] B. Song, M. Tang, E. Hu, O.J. Borkiewicz, K.M. Wiaderek, Y. Zhang, N.D. Phillip, X. Liu, Z. Shadike, C. Li, L. Song, Y.Y. Hu, M. Chi, G.M. Veith, X.Q. Yang, J. Liu, J. Nanda, K. Page, A. Huq, Understanding the low-voltage hysteresis of anionic redox in Na$_2$Mn$_3$O$_7$, Chem. Mater. 31 (2019) 3756–3765, https://doi.org/10.1021/acs.chemmater.9b00772.

[72] J. Liu, L. Yu, E. Hu, B.S. Guiton, X.Q. Yang, K. Page, Large-scale synthesis and comprehensive structure study of δ-MnO$_2$, Inorg. Chem. 57 (2018) 6873–6882, https://doi.org/10.1021/acs.inorgchem.8b00461.

[73] Y. Li, X. Wang, Y. Gao, Q. Zhang, G. Tan, Q. Kong, S. Bak, G. Lu, X. Yang, L. Gu, J. Lu, K. Amine, Z. Wang, L. Chen, Native vacancy enhanced oxygen redox reversibility and structural robustness, Adv. Energy Mater. 9 (2019), 1803087, https://doi.org/10.1002/aenm.201803087.

[74] K. Sada, B. Prabeer, Layered sodium manganese oxide Na$_2$Mn$_3$O$_7$ as an insertion host for aqueous zinc-ion batteries, MRS Adv. 4 (2019) 2651–2657, https://doi.org/10.1557/adv.2019.297.

[75] Z. Zhang, D. Wu, X. Zhang, X. Zhao, H. Zhang, Z. Xie, Z. Zhou, First-principles computational studies on layered Na$_2$Mn$_3$O$_7$ as a high-rate cathode material for sodium ion batteries, J. Mater Chem. A Mater. 5 (2017) 12752–12756, https://doi.org/10.1039/C7TA02609A.

[76] P. Zaccagnini, D. di Giovanni, M.G. Gomez, S. Passerini, A. Varzi, A. Lamberti, Flexible and high temperature supercapacitor based on laser-induced graphene electrodes and ionic liquid electrolyte, a de-rated voltage analysis, Electrochim. Acta 357 (2020), 136838, https://doi.org/10.1016/J.ELECTACTA.2020.136838.

[77] M. Khandelwal, C. van Tran, J. Lee, J. Bin, Nitrogen and boron co-doped densified laser-induced graphene for supercapacitor applications, Chem. Eng. J. 428 (2022), 131119, https://doi.org/10.1016/j.cej.2021.131119.